

Article

# Biochar Derived from Palm Waste Supported Greenly Synthesized MnO<sub>2</sub> Nanoparticles as a Novel Adsorbent for Wastewater Treatment

Amel Taha <sup>1,2,\*</sup>  and Samah Daffalla <sup>3,4</sup> <sup>1</sup> Department of Chemistry, King Faisal University, P.O. Box 400, Al-Ahsa 31982, Saudi Arabia<sup>2</sup> Department of Chemistry, Faculty of Science and Technology, Al-Neelain University, Khartoum 11121, Sudan<sup>3</sup> Department of Environment and Agricultural Natural Resources, College of Agricultural and Food Sciences, King Faisal University, P.O. Box 400, Al-Ahsa 31982, Saudi Arabia<sup>4</sup> Department of Chemical Engineering, College of Engineering, University of Khartoum, Khartoum P.O. Box 321, Sudan

\* Correspondence: ataha@kfu.edu.sa; Tel.: +966-135897506; Fax: +966-135899557

**Abstract:** Water pollution with dye effluents from different industries is a broadly established environmental and health problem that needs serious attention. In this study, making use of *Acacia nilotica* seed extract, greenly synthesized MnO<sub>2</sub> nanoparticles were loaded on the surface of biochar derived from palm waste (MnO<sub>2</sub>/PF), with specific surface areas of 70.97 m<sup>2</sup>/g. Batch experiments were adopted, aiming to evaluate the performance of palm fronds, biochar, and the MnO<sub>2</sub>/PF adsorbents in methyl orange (MO) removal from an aqueous solution. The feedstock and synthesized biochars were comprehensively characterized using XRD, SEM-EDX, FTIR, and BET surface area techniques. Moreover, the influences of the modification of palm fronds, initial dye concentrations, pH, and adsorbent dosage on MO uptake were examined. The results demonstrated that MnO<sub>2</sub>/PF biochar nanocomposite led to an increase in the removal efficiency by 6 and 1.5 times more than those of palm fronds and biochar, respectively. In addition, it was found that the second-order kinetic model presented the kinetic adsorption very well. This paper demonstrates that the depositing of greenly synthesized MnO<sub>2</sub> nanoparticles on the date palm waste biochar forms a novel adsorbent (MnO<sub>2</sub>/PF) for the removal of MO from aqueous solutions. Furthermore, this adsorbent was easy to synthesize under moderate conditions without the need for chemical capping agents, and would thus be cost-effective and eco-friendly.

**Keywords:** nanocomposites; date palm fronds; biochar; methyl orange; adsorption; MnO<sub>2</sub> nanoparticle synthesis



**Citation:** Taha, A.; Daffalla, S. Biochar Derived from Palm Waste Supported Greenly Synthesized MnO<sub>2</sub> Nanoparticles as a Novel Adsorbent for Wastewater Treatment. *Catalysts* **2023**, *13*, 451. <https://doi.org/10.3390/catal13020451>

Academic Editor: Marta Pazos Currás

Received: 24 January 2023

Revised: 9 February 2023

Accepted: 13 February 2023

Published: 20 February 2023



**Copyright:** © 2023 by the authors. Licensee MDPI, Basel, Switzerland. This article is an open access article distributed under the terms and conditions of the Creative Commons Attribution (CC BY) license (<https://creativecommons.org/licenses/by/4.0/>).

## 1. Introduction

Increasing environmental pollution is associated with the extensive uses of dyes in the cosmetics, leather, paper, printing, medicine, tannery, and textile finishing industries. Azo dyes comprise 60–70% of all of the inorganic dyes manufactured in the world, making them the largest group of colorants in textile effluents. Azo dyes, usually anionic, are amongst the most harmful types of dyes due to their high thermal, optical, and physico-chemical stability, since they have a stable chemical composition involving aromatic rings and azoic linkages. [1]. The high amount of dye-containing waste poses great challenges to the environment, since they have a strong color, high stability of complex structure, and resistance to biodegradability [2]. Therefore, it is very important to eliminate these dyes from wastewater to keep our aquatic life safe [1–3]. Among the most common azo anionic dyes is methyl orange (MO), which is widely used in different industries. MO is harmful to the environment and biology [3]. The various technologies that have been investigated for dye decontamination include adsorption, coagulation, and degradation technologies,

etc. [4–8]. Amongst these technologies, adsorption is found to be one of the better methods as it has a high efficiency, low cost and simple operation [9]. Different materials have been used to ensure the economic feasibility of the wastewater treatment process, such as agricultural waste, since it is abundantly available and renewable [10]. Water lettuce, agrowastes, *Nepenthes rafflesiana* pitcher, and leaves were also used as potential adsorbents for acid blue 25 (AB25) and methyl violet 2B (MV) dye removal, respectfully [11,12].

Adsorption onto biochars derived from biomass is considered an effective and environmentally friendly method to remove many of the contaminants from wastewater [13–15]. Biochar can be produced from biomass using thermochemical and biochemical technologies. However, the thermochemical process using low pyrolysis is one of the most effective and efficient processes to get biochar from biomass [16]. Biochar production through pyrolysis is affected by different parameters such as temperature, pressure, reaction time, nitrogen flow, and others. These parameters control the char yield, the nature of the active sites, and the pore characteristics of biochar. Along with these operating parameters, the structure of the biomass also influences the product yield [16–19]. The agricultural economy of the Kingdom of Saudi Arabia is dominated by the export and production of dates, and date trees represent a large amount of waste that is disposed of in a large volume. Dates are a by-product of date palm trees, which are produced in large quantities. In fact, it is estimated that more than thousands of tons of palm waste are generated annually [19]. This waste is not used effectively, as the waste is generally collected and transported to a landfill, potentially creating pollution to the surrounding environments. Therefore, due to the abundant availability of palm waste, it is essential to examine the possibility of utilizing it as an effective material in treating wastewater. Thus, converting this biomass waste to high value biochar product can minimize solid waste handling and reduce the impact on the environment.

Biochar is considered to be a supreme feature material as it has a highly rich carbon content, a large specific surface area, a high porosity with many different functional groups, and is highly available with a low cost as a raw material [16]. Furthermore, due to their abundant functional groups and large chemical and electrical stability, biochars can serve as an interesting support for metal nanoparticles [20]. Recently, syntheses of biochar nanocomposites have been used by many researchers due to the biochar porous structure and the properties of nanoparticles, for the removal of dyes from wastewater [20–22]. Thus, the modification of the biochar surface area with  $\text{MnO}_2$  nanoparticles makes the production of new composites such as  $\text{MnO}_2/\text{PF}$  an efficient economic catalyst for the removal of contaminants, since it increases the active site of the biochar [23].

Metal nanoparticles are in need of great attention because of their varied applications and morphology-dependent characteristics [20]. They have attracted significant attention from researchers due to these possible applications and novel characteristics [24]. Manganese oxide has been used as an efficient adsorbent material for the elimination of numerous harmful contaminants from wastewater. From the environmental perspective, a synthesis of a biochar nanocomposite with a high surface area and surface active sites from palm waste for the adsorption of dyes from wastewater is considered effective and eco-friendly. A biogenic synthesis of manganese oxide nanoparticles using plant-based techniques has numerous advantages, including one-pot synthesis, an economical, eco-safe approach of eliminating the uses of hazardous and toxic reducing agents such as of sodium borohydride. Furthermore, the use the plant's biomolecules as a reducing and capping agent leads to a lower aggregation and uniforms the particles' shape [25].

In this work, *Acacia nilotica* pod extract was used as a reducing agent for the formation of manganese oxide nanoparticles. *A. nilotica* is a tropical plant related to the family of Leguminosae-Mimosoideae. It has been traditionally used as a treatment of various diseases, such as cough, diarrhea, cancer, and others. *A. nilotica* contains numerous biomolecules such as alkaloids, flavonoids, phenolic compounds, and saponins [26–28], which can work as a reducing and stabilizing agent for  $\text{Mn}^{+2}$  ions. Due to dye contamination problems, it is important to develop a new adsorbent material for dye removal from

wastewater, as it is an environmental concern. In this regard, so far, no reports have been stated on the synthesis of the  $\text{MnO}_2$ /PF biochar nanocomposite as an adsorbent for dye removal. Thus, in this work, an effective and eco-friendly adsorbent will be prepared by the combination of biochar derived from date palm waste (PF) to support  $\text{MnO}_2$  nanoparticles, which were prepared using *A. nilotica* pod extract as a stabilizing and capping agent under very mild conditions, as an environmental material for the adsorption of MO. The influence of different adsorbent parameters was evaluated and the kinetic data was studied in terms of pseudo-first- and second-order models.

## 2. Results and Discussion

### 2.1. Characterization of Adsorbents

#### 2.1.1. XRD Analysis

To investigate the phase purity and the crystallinity of the prepared samples, the XRD technique was used, and the results are presented in Figure 1. The characteristic peaks in the XRD pattern for the palm waste raw material (Figure 1a) indicate the existence of a broad peak at  $22.06^\circ$   $2\theta$  of a carbon-containing mineral mellite ( $\text{Al}_2[\text{C}_6(\text{COO})_6 \cdot 16\text{H}_2\text{O}]$ ). Ju et al. [29] obtained similar results at  $20.53^\circ$   $2\theta$  with bleach wood pulp, while Munir et al. [30] reported that date palm waste has this broad peak at  $21.48^\circ$   $2\theta$ . This biomass in palm waste was lost during the pyrolysis, as shown in Figure 1b,c. Figure 1 shows that the major crystalline peaks of the biochar from the palm waste were quartz ( $\text{SiO}_2$ ) peaks at  $2\theta$ :  $29.16^\circ$ ,  $37.24^\circ$ , and  $43.32^\circ$  and a calcite ( $\text{CaCO}_3$ ) peak at  $64.16^\circ$ ,  $76.8^\circ$ , and  $81.04^\circ$   $2\theta$  [31,32]. These peaks were still present, even after pyrolysis. Figure 1c shows the distinguishing peaks of the Mn nanoparticles in the  $\text{MnO}_2$ /PF biochar nanocomposite in  $2\theta$  values at  $18.48^\circ$ ,  $29.04^\circ$ ,  $37.04^\circ$ ,  $50.44^\circ$ ,  $60.36^\circ$ , and  $65.08^\circ$ , indexed to (200), (310), (301), (411), (521), and (002) crystal planes, respectively [33,34]. These diffraction peaks confirm the presence of the  $\alpha$ - $\text{MnO}_2$  crystal phase according to JCPDS no. 44-0141 standard data [35].

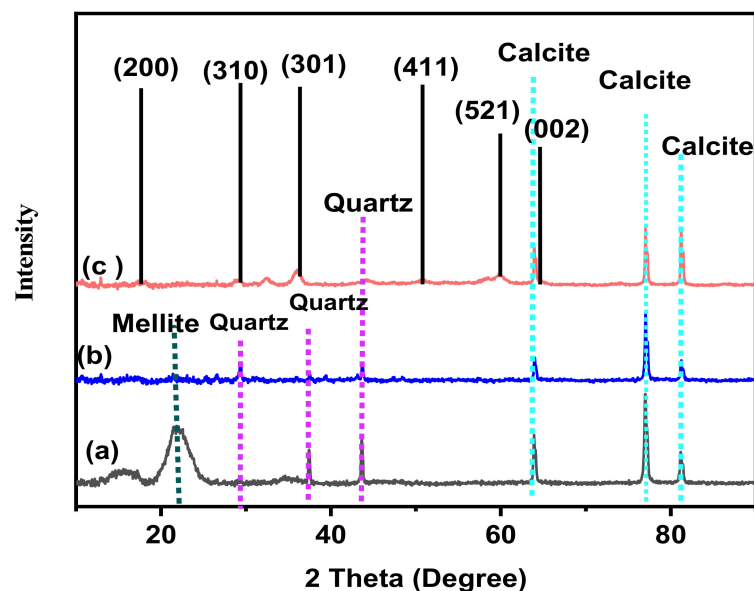
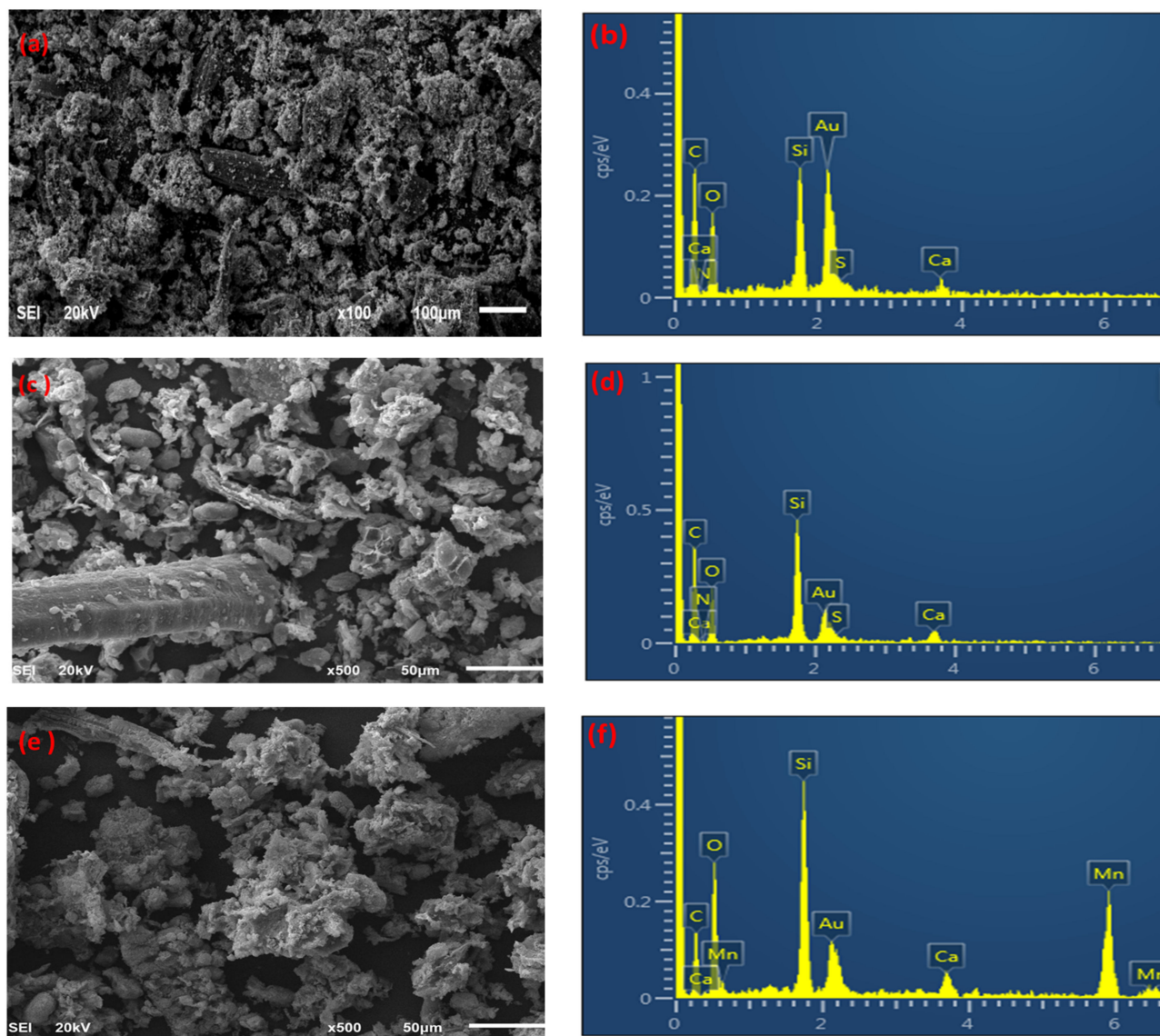


Figure 1. XRD spectra of (a) palm waste, (b) biochar, and (c)  $\text{MnO}_2$ /PF biochar nanocomposite.

#### 2.1.2. SEM-EDX Studies

The morphology of palm waste raw material, biochar, and the  $\text{MnO}_2$ /PF biochar nanocomposite were studied using scanning electron microscope analysis (SEM), as shown in Figure 2a,c,e. The palm waste raw material showed a cross-linked structure (Figure 2a). This cross-linking was due to the presence of a network containing lignin, a cellulose in biomass. After pyrolysis, few pores were seen in the raw material when compared to its biochar [30]. It was also observed that the surface of the biochar was rougher than the

raw palm waste biomass (Figure 2c), and porous structures were formed on the surface, which was caused by the volatilization of organic materials [36]. Figure 2e displays the aggregation of the MnO<sub>2</sub> nanoparticles on the biochar surface.



**Figure 2.** SEM and EDX for palm waste (a,b), biochar (c,d), and MnO<sub>2</sub>/PF biochar (e,f).

EDX analysis was used to investigate the elemental composition present in the palm waste, its biochar, and the MnO<sub>2</sub>/PF biochar nanocomposite. Figure 2b,d,f show the presence of different elements on the materials for the raw palm waste, biochar, and MnO<sub>2</sub>/PF biochar nanocomposite. The EDX spectra (Figure 2b,d,f) show characteristic peaks which are corresponding to carbon, oxygen, silicon and calcium. These EDX peaks are attributed to the quartz and calcite composition of the raw material and its biochar [37,38], while the presence of manganese element on the MnO<sub>2</sub>/PF biochar nanocomposite surface confirmed the effective synthesis of the MnO<sub>2</sub> NPs [39]. The presence of Au peaks originates from the Au coating, which was performed to minimize the surface electron charging via the EDS [40].

### 2.1.3. FTIR Analysis

The FTIR spectra of the palm waste, biochar and MnO<sub>2</sub>/PF are shown in Figure 3. The spectrum showed that the palm waste functional groups are changed clearly during the pyrolysis process (Figure 3a). The presence of OH stretching at 3347 cm<sup>-1</sup> in the palm

waste spectrum is dominated by the bonded water and other volatile functional groups, which are obviously decreased in the biochar (Figure 3b) [30]. The presence of peaks at 2855 and 2914  $\text{cm}^{-1}$  or aliphatic C–H stretch in the palm waste is due to the presence of organic molecules, which disappear into the biochar and  $\text{MnO}_2/\text{PF}$ . Figure 3b,c suggests that these organic molecules were removed from the palm waste after the pyrolysis process. Furthermore, it is noticed that the band at 1625  $\text{cm}^{-1}$  for carboxylic acids tends to disappear after the pyrolysis in the biochar and  $\text{MnO}_2/\text{PF}$  spectrum. The same results were obtained by Chun et al. [41], in which they confirm a reduction in the amount of acidic groups COOH, with an increase in the pyrolysis temperature and even a disappearance at high temperature. The presence of the peak at 1088  $\text{cm}^{-1}$  in all three spectrums can be attributed to the Si–O–Si [30]. Additionally, the presence of a new  $\text{MnO}_2$  peak was detected at 611  $\text{cm}^{-1}$ , only in  $\text{MnO}_2/\text{PF}$ , approving the formation of the  $\text{MnO}_2$  nanoparticles. Therefore, this result confirmed the successful formation of the  $\text{MnO}_2/\text{PF}$  [42].

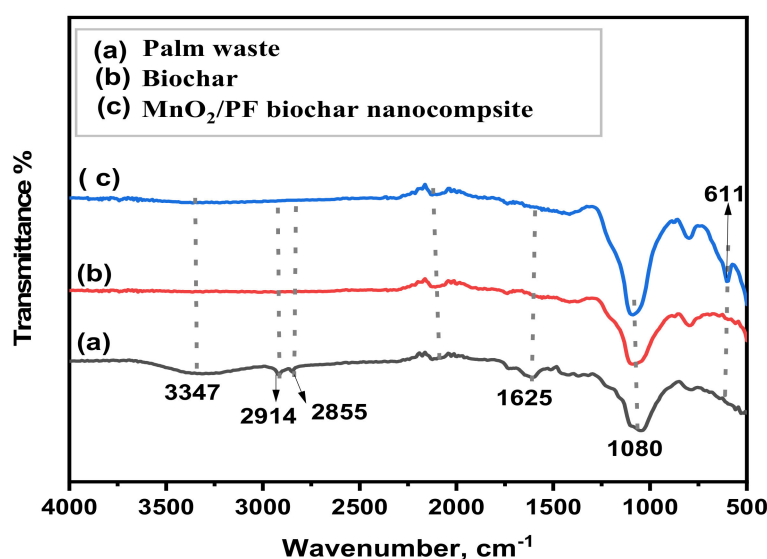


Figure 3. FTIR spectrum of (a) palm waste, (b) biochar, and (c)  $\text{MnO}_2/\text{PF}$  biochar nanocomposite.

#### 2.1.4. BET Analysis

The nitrogen adsorption–desorption isotherm of the palm fronds, biochar, and  $\text{MnO}_2/\text{PF}$  biochar is presented in Figure 4. This figure shows that the palm fronds and biochar possessed type II and IV isotherms with an H3 hysteresis loop [43], indicating the presence of macroporous and mesopores structures, while the  $\text{MnO}_2/\text{PF}$  biochar adsorbent possessed a type IV isotherm with an H3 hysteresis loop, which is characteristic of a solid with a mesoporous structure [43]. On the other hand, the textural properties of the adsorbents are tabulated in Table 1. Moving from palm waste to the  $\text{MnO}_2/\text{PF}$  biochar, significant increases in the surface area and average pore diameter were confirmed. It was found that the surface area of the  $\text{MnO}_2/\text{PF}$  biochar was 153 and 41 times more than those of the palm fronds and biochar, respectively, while the average pore diameter of the palm fronds was increased from 0.0018  $\text{cm}^3/\text{g}$  to 0.0123  $\text{cm}^3/\text{g}$  and 0.1363  $\text{cm}^3/\text{g}$  for the biochar and  $\text{MnO}_2/\text{PF}$  biochar, respectively. Moreover, as seen in Table 1, for all the samples, the average pore size diameter was in the range of 11–48 nm. This confirms that the studied samples have mesoporous structures.

#### 2.1.5. Biochar Yield of Pyrolysis

The yield of the low pyrolysis biochar produced at 600 °C was calculated using Equation (1). It was found that the biochar yield for the palm fronds was 38.46%. The biochar yield is affected by the pyrolysis process parameters (temperature, reaction time, and nitrogen flow), as well as the inert and lignin contents of the biomass [44].

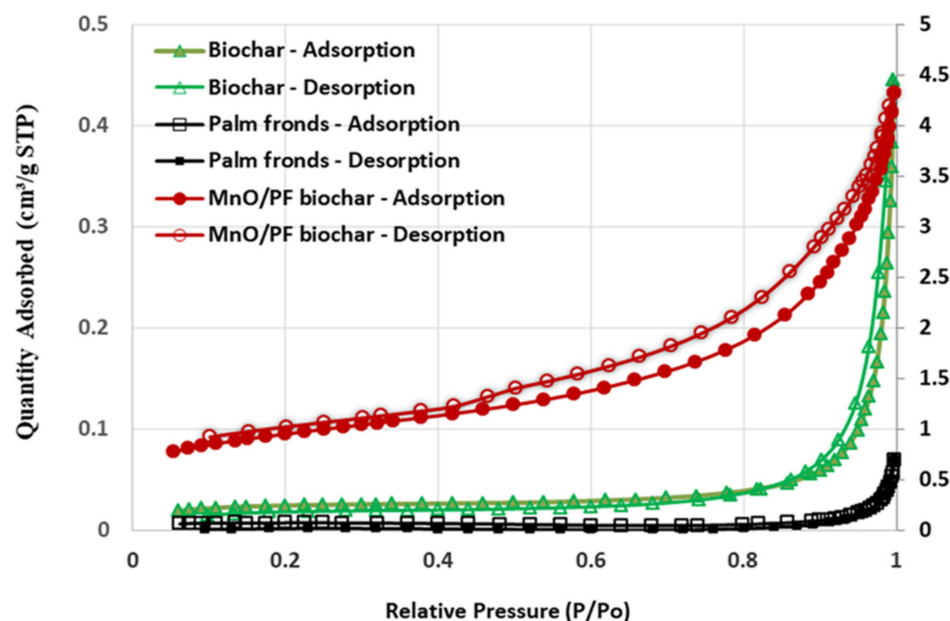


Figure 4. Hysteresis loops of palm fronds, biochar, and MnO<sub>2</sub>/PF biochar.

Table 1. Pore textural characteristics of palm fronds, biochar, and MnO<sub>2</sub>/PF biochar.

Sample	BET Surface Area (m <sup>2</sup> /g)	Total Pore Volume (cm <sup>3</sup> /g)	Average Pore Diameter (nm)
Palm fronds	0.463	0.0018	48.42
Biochar	1.74	0.0123	45.53
MnO <sub>2</sub> /PF biochar	70.97	0.1363	11.17

## 2.2. Batch Adsorption Studies

### 2.2.1. Effect of Adsorbent Type on MO Uptake

The adsorption behavior of the palm fronds, biochar, and MnO<sub>2</sub>/PF biochar nanocomposite was studied. A total of 0.07 g of each adsorbent was added to the 10 mg/L initial MO solution at pH 2.0 and 25 °C for 24 h. The results demonstrated that the MnO<sub>2</sub>/PF biochar has the highest removal efficiency, which is 6 and 1.5 times more than those of the palm fronds and biochar, respectively. Hence, the MnO<sub>2</sub>/PF was selected for further studies.

### 2.2.2. Effect of pH

The pH of the MO solution has a significant effect on its removal because it has great influences on the adsorbent surface's properties, as well as the ionization degree of the MO. [45]. To estimate the influence of the solution pH on the MO sorption, an experiment was conducted at different pH values, ranging from 2.0 to 11.0 and keeping the MO initial concentration of 10 mg/L, contact time of 24 h, and 0.07 g dose of MnO<sub>2</sub>/PF fixed. As shown in Figure 5, at pH 2.5, the MO removal efficiency reached the maximum value of 91.5%. With the increasing in the pH of the solution from pH 4 to 11, it was noticed that the value of the adsorption percentage (RE %) decreased. A very weak percentage of the removal efficiency (29%) was detected when the solution pH was higher than 10. This could be due to the high deprotonation of the MnO<sub>2</sub>/PF surface, which, accordingly, will bear a negative charge. Therefore, a strong repulsive force will happen between the MO anions and the negative adsorbent surface, and thus delay the MO reaching the MnO<sub>2</sub>/PF surface [46]. In contrast, when the solution pH decreased, the MnO<sub>2</sub>/PF surface became positively charged and attracted the negative MO anions, leading to a higher removal efficiency. Similar results have been reported by many researchers on the adsorption of MO onto various adsorbents [47–49]

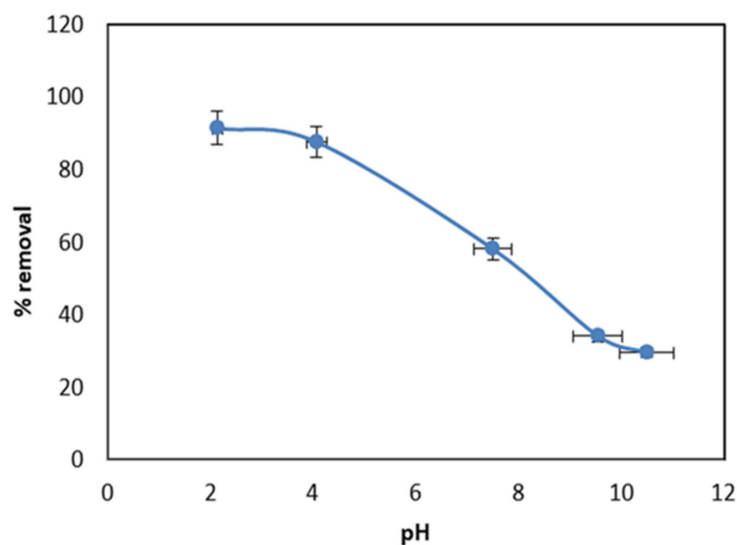


**Figure 5.** Effect of solution pH on MO uptake by  $\text{MnO}_2/\text{PF}$  biochar at contact time, 24 h; initial concentration of MO, 10 mg/L; and 0.07 g of  $\text{MnO}_2/\text{PF}$ .

### 2.2.3. Effect of MO Initial Concentration

Figure 6 demonstrates the effect of different MO concentrations, varying from 10 to 50 mg/L at pH 2.5, 0.07 g adsorbent dose, and 25 °C. From Figure 6, it is clear that with the increase in the MO initial concentration, the removal efficiency decreased. The higher removal efficiency was 91.5% for 10 mg/L, and with further increases in the initial concentration, the removal percentage decreased to 61.9% for 50 mg/L. This is owing to the limitation of the active site on the  $\text{MnO}_2/\text{PF}$  surface, since the amount of adsorbent was kept constant while the initial concentration was increased from (10–50 mg/L). Additionally, the increase in the MO concentration makes the active sites on the  $\text{MnO}_2/\text{PF}$  biochar adsorbent saturated very fast, so there is no available active site on the adsorbent surface for the MO molecules to react with. Similar observations were reported by Hemamalathi et al. [41] and Lu Han et al. [42]. However, the adsorption capacity increased from 2.61 to 9.11 mg/g with the increase in the initial concentration of MO from 10 to 50 mg/L (Figure 6). This is because of the increase in the mass transfer driving force, with an increase the initial concentration of the solution.

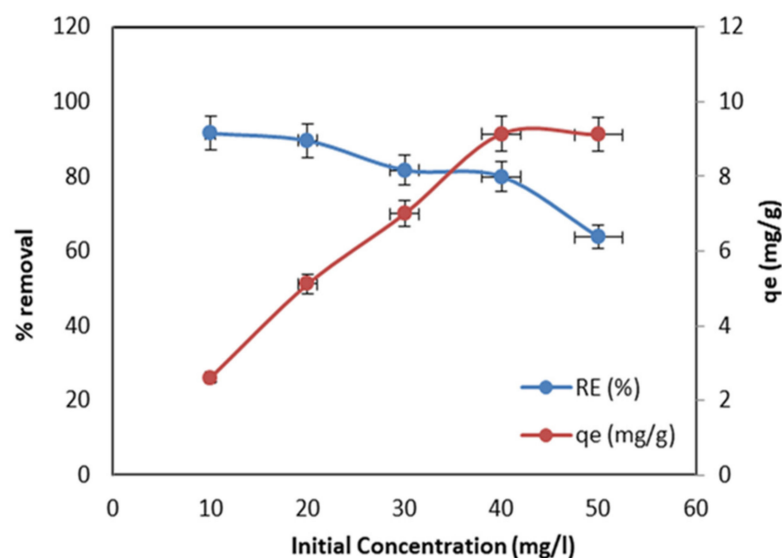


**Figure 6.** Effect of different MO concentrations on adsorption capacity and removal efficiency (pH 2.5; 0.07 g, adsorbent dose; and 24 h, contact time).

#### 2.2.4. Effect of MnO<sub>2</sub>/PF Biochar Dose

Figure 7 shows the effect of the various masses of the MnO<sub>2</sub>/PF biochar nanocomposite, ranging between 0.01 and 0.1 g with the MO removal efficiency and adsorption capacity ( $q_e$ ). The selected mass was mixed with 20 mL of the 10 mg/L Cr (VI) solution at pH 2.5 and 25 °C. In Figure 7, it is demonstrated that, with increase in dose amount, the MO removal efficiency increased, while the adsorption capacity of the MnO<sub>2</sub>/PF decreased. It can be seen that, with the increase in the adsorbent dosage from 0.01 to 0.07 g, there was a considerable increase in the removal percentage of MO, from 59.4% to 91.5%, possibly owing to an increase in the number of adsorption active sites [50]. However, the higher doses of the MnO<sub>2</sub>/PF result in a lowering of the removal percentage of MO to 37.72%. In fact, at the low dosage of adsorbent, there will be a well dispersion of the MnO<sub>2</sub>/PF biochar in an aqueous solution, so that all the MnO<sub>2</sub>/PF surface active sites are uncovered, which can increase the affinity of the MO molecules to the MnO<sub>2</sub>/PF active sites. Therefore, the active sites of the adsorbent are quickly saturated, resulting in a high removal percentage. Conversely, the higher adsorbent dosages make the availability of the higher energy adsorbent active sites decrease, and occupy a large fraction of the active sites with lower energy, which decrease with the adsorption removal. Additionally, when the adsorbent doses increase, it leads to particle aggregation, due to the collision between the adsorbent nanoparticles which reduce the total surface area, which results in a decrease in the percentage removal of the MO from an aqueous solution. Therefore, the optimal dosage (0.07 g) was selected for the rest of the study [50]. On the other hand, it was found that the adsorption capacity values of the MnO<sub>2</sub>/PF biochar nanocomposite were gradually decreasing upon the increasing the adsorbent dosage, suggesting that higher numbers of adsorbent functional groups are available compared to the number of interacting MO.

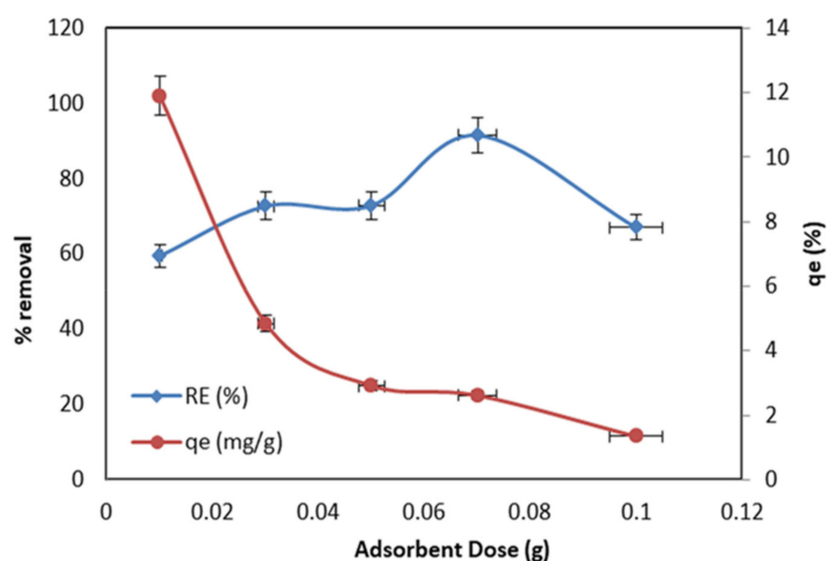


**Figure 7.** Effect of MnO<sub>2</sub>/PF biochar dosage on the removal of MO adsorption capacity and removal efficiency (pH 2.5; 10 mg/l, initial MO concentration; and 24 h, contact time).

#### 2.3. Effect of Surface Functional Groups on MO Adsorption

The effects of surface functional groups on MO adsorption were analyzed by observing the shifting of the FTIR peaks after the adsorption experiment. The identified peaks for the MnO<sub>2</sub>/PF biochar, both before and after the sorption experiment, are tabulated in Table 2. As shown in this table, some of the FTIR peaks of the MnO<sub>2</sub>/PF biochar after the adsorption experiment have shifted, particularly at the lower and higher wave numbers. Based on this observation, it can be stated that the carbon functional groups (C–H, C=C, C–O, C=O and C≡C) contribute to the adsorption of MO onto the surface of the MnO<sub>2</sub>/PF biochar.

**Table 2.** FTIR spectra of MnO<sub>2</sub>/PF biochar before and after MO sorption (*I*, before MO sorption and *II*, after MO sorption).

MO Sorption	Functional Group			
	C–H, C=C	C–O	C=O	C≡C
<i>I</i>	797	1080	1625	2102
<i>II</i>	790	1073	1685	2109

#### 2.4. Kinetics Analysis

Kinetics studies were performed using 20 mL of 10 mg/L of methyl orange and 0.02 g of the adsorbent dose, at the optimum pH of 2.5. The kinetic behavior of MO onto the MnO<sub>2</sub>/PF biochar nanocomposite was calculated in terms of pseudo-first- and second-order models. Based on the linear regression correlation coefficient values ( $R^2$ ), the best-fit model was selected. The first-order kinetic model can be presented by the following equation [51].

$$\ln(q_e - q_t) = \ln q_e - k_1 t \quad (1)$$

where  $q_e$  and  $q_t$  (mg/g) are the amount of MO adsorbed at equilibrium and time  $t$ , respectively, and  $k_1$  is the rate constant of the pseudo-first-order kinetic model ( $\text{min}^{-1}$ ) and  $t$  time (min).

A linear form of the second-order kinetic model can be presented by the following form [51].

$$\frac{t}{q_t} = \frac{1}{k_2 q_e^2} + \frac{1}{q_e} t \quad (2)$$

where  $k_2$  (g/mg·min) is the second-order kinetic rate constant.

The results of the two models are presented in Supplementary Figure S1 and their kinetic coefficients in Table 3. From Table 3 and Supplementary Figure S1, the pseudo-second-order shows higher value correlation coefficients,  $R^2$  (0.995), than the pseudo-first-order (0.723). Moreover, it was found that there is a good agreement between the experimental ( $q_{e,\text{exp}}$  10.71 mg/g) and calculated values for the pseudo-second-order ( $q_{e,\text{cal}}$  9.61 mg/g), while the  $q_{e,\text{cal}}$  value for the pseudo-first-order is 5.46 mg/g, proposing that the adsorption kinetic is well described by the pseudo-second-order.

**Table 3.** Pseudo-first-order and second-order coefficient.

Model	Parameters	
	$q_{e,\text{exp}}$ (mg/g)	10.71
Pseudo-first order	$q_{e,\text{cal}}$ (mg/g)	5.46
	$k_1$ ( $\text{min}^{-1}$ )	0.0196
	$R^2$	0.7229
Pseudo-second order	$q_{e,\text{cal}}$ (mg/g)	9.61
	$k_2$ (g/mg·min)	0.028
	$R^2$	0.9951

Previously, some researchers demonstrated the applicability of the pseudo-second-order kinetic model to describe the adsorption process of MO onto various adsorbents. By comparing the results obtained in this study with those in previously reported works (Table 4) on the adsorption mechanism of various adsorbents in aqueous solutions for MO, it is clear that similar phenomena have been observed for the adsorption mechanism of MO onto the MnO<sub>2</sub>/PF biochar.

**Table 4.** Previously reported kinetic studies of various adsorbents for MO.

Adsorbent	Parameters		Reference
	$k_2$ (g/mg. min)	$R^2$	
Multiwalled carbon nanotubes	0.00457	0.9980	[52]
AC derived from phragmites australis	0.000016	0.9999	[53]
AC derived from pomelo peel waste	0.000683	0.9840	[54]
Chitosan wrapping magnetic nanosized and multi-walled carbon nanotubes	0.02340	0.9980	[55]
NiO nanoparticles	0.00076	0.9890	[24]
CuO nanoparticles	0.02441	0.9980	[56]
Polyaniline-kapok fiber nanocomposite	0.00012	0.9980	[56]
MnO <sub>2</sub> /PF biochar	0.02800	0.9951	<b>This study</b>

### 3. Materials and Methods

#### 3.1. Materials

The date palm fronds were obtained freely from a local farm in Al-Ahsa, Saudi Arabia. Mn (MnCl<sub>2</sub>·4H<sub>2</sub>O 98% Merck) was used for the synthesis of the MnO<sub>2</sub>/PF biochar nanocomposite. The solution pH was controlled using hydrochloric acid (0.1 M HCl, Merck) and sodium hydroxide (0.1 M NaOH Merck). Methyl orange (98% MO Merck) was used to evaluate the adsorption process.

#### 3.2. Preparation of *Acacia Nilotica* Extract

The pods of *A. nilotica* were collected from Hofuf local markets in Saudi Arabia. To prepare the extract, the pods were rinsed extensively using tap and distilled water to make sure any dusts and impurities were removed. In total, 10 g of *A. nilotica* pods was boiled for 15 min at 100 °C in distilled water. The extract was centrifuged at 10,000 rpm for 10 min using the centrifuge model XC-L6Z, and the supernatant was collected and then filtered.

#### 3.3. Synthesis of PF Biochar

The PF sample was first washed many times using distilled water in order to eliminate any impurities, and then after drying for 24 h, the dried PF was ground lightly using a grinding machine. The milled palm frond particles of sizes between 250–125 µm were selected for biochar production. About 60 g of the grinded PF was then pyrolyzed in a tubular furnace at 600 °C under nitrogen flow at 200 mL/min for 60 min, with a 10 °C/min heating rate. The slow pyrolysis at a temperature of 600 °C was selected based on its characterization of a slow heating rate and long residence time [57].

#### 3.4. Synthesis of MnO<sub>2</sub>/PF Biochar Nanocomposite

Figure 8 shows the steps of the MnO<sub>2</sub>/PF biochar nanocomposite synthesis. A total of 2.5 g of the PF biochar was mixed with 100 mL of 0.1 M MnCl<sub>2</sub>·4H<sub>2</sub>O solution, and then 20 mL of the *A. nilotica* was added to the blend and continuously stirred for 30 min. The pH of the mixture was adjusted at 11 using 1 M KOH and an Orion 2-star pH meter. The mixture was then left to be stirred at room temperature and 70 rpm for 24 h. Then, the blend was filtered and the solid was rinsed with distilled water and then ethanol. Finally, it was dried at 40 °C and was subject to calcination at 200 °C for 3 h.



**Figure 8.** Schematic diagram of the synthesis of MnO<sub>2</sub>/PF biochar nanocomposite.

### 3.5. Characterization

The morphological structures of the PF and the prepared MnO<sub>2</sub>/PF biochar nanocomposite were assessed using field-emission scanning electron microscopy (FE-SEM model JSM-7610F, JEOL, Peabody, MA, USA), fitted with an X-ray energy dispersive spectroscopy system EDX. The surface area and pore structure were analyzed using a Brunauer–Emmett–Teller (BET) surface area analyzer (a NOVA 4200e (Quantachrome Instruments, B Beach, FL, USA)). Fourier transform infra-red (FTIR) was performed with Thermo Scientific, Quattro S, Guilford, CT, USA) which was used to confirm the presence of functional groups. The crystal structure of the prepared MnO<sub>2</sub>/PF biochar nanomaterial was studied using an X-ray diffractometer with a wavelength of 1.54 Å, (XRD-7000 with a Cu-detector Shimadzu, Tokyo, Japan) over the 2θ range of 10–80°. The yield of the developed biochar was calculated using Equation (1).

$$\text{Biochar yield (\%)} = \frac{\text{mass of biochar}}{\text{mass of dried palm fronds}} \times 100 \quad (3)$$

### 3.6. Adsorption Experiment

The adsorption of the MO using the MnO<sub>2</sub>/PF biochar nanocomposite was conducted under different conditions with continuous stirring at 80 rpm. The batch experiment was carried out in an Erlenmeyer flask (50 mL) with 20 mL of the 10 mg/L initial MO concentration at pH 2.5 and 298 K. The pH (2–11) of the solution was adjusted using 0.5 M HCl and 0.5 M NaOH. The evaluated concentration ranged between 10 and 50 mg/L. To study the effect of the adsorbent dose on MO adsorption, various doses of MnO<sub>2</sub>/PF, ranging between 0.01 and 0.1 g, were added to the 20 mg/L initial MO concentration at 298 K and pH 2.5. In the experiment on the effect of the initial dye concentration, the evaluated concentration varied from 10 to 50 mg/L at pH 2.5. Aqueous samples were collected at certain time periods and filtered using Whatman No.1 filter paper. The filtrate was used to calculate the maximum absorbance of the MO solution at a wavelength of 464 nm, using the UV-vis spectrophotometer (Shimadzu, Kyoto, Japan). A kinetic study was conducted at pH 2.5. The MO concentrations were analyzed after 0, 2, 5, 10, 15, 20, 30, 40, 50, 60, 90, and 120 min. All of the experiments were performed two times, and the

average of the values was used in the study. The MO removal percentage and adsorption capacity were calculated with Equations (2) and (3),

$$\% \text{ removal of MO} = \frac{(C_o - C_t)}{C_o} \times 100 \quad (4)$$

$$\text{Adsorption capacity } (q_e) = \frac{(C_o - C_e)V}{W}, \text{ (mg of adsorbate/g of adsorbent)} \quad (5)$$

where  $C_t$  (mg/L) is the MO concentration at time  $t$ , and  $C_o$  (mg/L) is the initial concentration of the MO solution.  $C_e$  (mg/L) is the equilibrium concentration of MO,  $V$  is the volume of the MO solution (L), and  $W$  is the mass of the adsorbent (g).

#### 4. Conclusions

The biochar derived from palm-waste-supported MnO<sub>2</sub> nanoparticles (MnO<sub>2</sub>/PF) was successfully synthesized by employing *Acacia nilotica* seed extract as a stabilizing and capping agent. The different properties of the palm fronds and developed biochars were characterized by FT-IR, SEM-EDX, XRD, and BET analysis. The adsorption studies of the MnO<sub>2</sub>/PF biochar nanocomposite were investigated in a batch mode at pH (2–11), an initial MO concentration of (10–50 mg/L), and an adsorbent dose of (0.01–0.1 g). It was found that the MnO<sub>2</sub>/PF biochar showed the highest micro-mesopores structure and surface area (70.97 m<sup>2</sup>/g), compared to those of other samples. Furthermore, the morphological features of the biochar samples showed that porous structures were formed on the surface, which were caused by the volatilization of organic materials. In addition, the FTIR analysis showed that these functional groups (C–H, C=C, C–O, C=O and C≡C) contributed to the adsorption of MO onto the surface of the MnO<sub>2</sub>/PF biochar. The results also demonstrated that the highest removal efficiency (91.5%) was observed at a pH value of 2.5, while the raw material and biochar showed low uptake efficiencies at a pH of 2.5 (14.7% and 62.7%), respectively. According to the kinetics experiments, the adsorption of MO onto the MnO<sub>2</sub>/PF biochar nanocomposite followed pseudo-second-order kinetics. It can be concluded that the MnO<sub>2</sub>/PF biochar nanocomposite synthesized from palm fronds could effectively adsorb MO from aqueous solutions.

**Supplementary Materials:** The following supporting information can be downloaded at <https://www.mdpi.com/article/10.3390/catal13020451/s1>, Figure S1: (a) pseudo-first order model, and (b) pseudo-second order model for adsorption of MO onto MnO<sub>2</sub>/PF biochar.

**Author Contributions:** Conceptualization, methodology, validation, formal analysis, investigation, resources, data curation, and visualization, A.T. and S.D.; supervision, project administration, writing—original draft preparation, and funding acquisition, A.T. and D.S; software, and writing—review and editing, A.T. and S.D. All authors have read and agreed to the published version of the manuscript.

**Funding:** This research was funded by the Deputyship for Research & Innovation, Ministry of Education in Saudi Arabia through project number INST063.

**Data Availability Statement:** Data only available upon request from corresponding author.

**Acknowledgments:** The authors extend their appreciation to the Deputyship for Research & Innovation, Ministry of Education in Saudi Arabia for funding this research work through the project number INST063.

**Conflicts of Interest:** The authors declare no conflict of interest.

#### References

1. Foster, S.L.; Estoque, K.; Voecks, M.; Rentz, N.; Greenlee, L.F. Removal of synthetic azo dye using bimetallic nickel-iron nanoparticles. *J. Nanomater.* **2019**, *2019*, 9807605. [CrossRef]
2. Vats, S.; Srivastava, S.; Maurya, N.; Saxena, S.; Mudgil, B.; Yadav, S.; Chandra, R. Advances in dye contamination: Health hazards, biodegradation, and bioremediation. In *Biological Approaches to Controlling Pollutants*; Woodhead Publishing: Sawston, UK, 2022; pp. 139–162.

3. Hamad, H.N.; Idrus, S. Recent developments in the application of bio-waste-derived adsorbents for the removal of methylene blue from wastewater: A review. *Polymers* **2022**, *14*, 783. [[CrossRef](#)] [[PubMed](#)]
4. Vishnu, D.; Dhandapani, B.; Authilingam, S.; Sivakumar, S.V. A comprehensive review of effective adsorbents used for the removal of dyes from wastewater. *Curr. Anal. Chem.* **2022**, *18*, 255–268. [[CrossRef](#)]
5. Patil, R.; Zahid, M.; Govindwar, S.; Khandare, R.; Vyavahare, G.; Gurav, R.; Desai, N.; Pandit, S.; Jadhav, J. Constructed wetland: A promising technology for the treatment of hazardous textile dyes and effluent. In *Development in Wastewater Treatment Research and Processes*; Elsevier: Amsterdam, The Netherlands, 2022; pp. 173–198.
6. Chinedu Egbosiuaba, T. Application of Agricultural Waste in Anionic Dyes Removal from Wastewater. In *Textile Wastewater Treatment: Sustainable Bio-Nano Materials and Macromolecules*; Springer Nature: Singapore, 2022; Volume 2, pp. 111–141.
7. Jagaba, A.H.; Kutty, S.R.; Isa, M.H.; Affam, A.C.; Aminu, N.; Abubakar, S.; Noor, A.; Lawal, I.M.; Umaru, I.; Hassan, I. Effect of environmental and operational parameters on sequential batch reactor systems in dye degradation. In *Dye Biodegradation, Mechanisms and Techniques: Recent Advances*; Springer: Singapore, 2022; pp. 193–225.
8. Alsukaibi, A.K. Various approaches for the detoxification of toxic dyes in wastewater. *Processes* **2022**, *10*, 1968. [[CrossRef](#)]
9. Iwuozor, K.O.; Ighalo, J.O.; Emenike, E.C.; Ogunfowora, L.A.; Igwegbe, C.A. Adsorption of methyl orange: A review on adsorbent performance. *Curr. Res. Green Sustain. Chem.* **2021**, *4*, 100179. [[CrossRef](#)]
10. Gupta, V.K.; Nayak, A. Cadmium removal and recovery from aqueous solutions by novel adsorbents prepared from orange peel and Fe<sub>2</sub>O<sub>3</sub> nanoparticles. *Chem. Eng. J.* **2012**, *180*, 81–90. [[CrossRef](#)]
11. Kooh, M.R.; Dahri, M.K.; Lim, L.B. Removal of methyl violet 2B dye from aqueous solution using *Nepenthes rafflesiana* pitcher and leaves. *Appl. Water Sci.* **2017**, *7*, 3859–3868. [[CrossRef](#)]
12. Kooh, M.R.; Dahri, M.K.; Lim, L.B.; Lim, L.H.; Chan, C.M. Separation of acid blue 25 from aqueous solution using water lettuce and agro-wastes by batch adsorption studies. *Appl. Water Sci.* **2018**, *8*, 61. [[CrossRef](#)]
13. Mrozik, W.; Minofar, B.; Thongsamer, T.; Wiriyaphong, N.; Khawkomol, S.; Plaimart, J.; Vakros, J.; Karapanagioti, H.; Vinitnantharat, S.; Werner, D. Valorisation of agricultural waste derived biochars in aquaculture to remove organic micropollutants from water—experimental study and molecular dynamics simulations. *J. Environ. Manag.* **2021**, *300*, 113717. [[CrossRef](#)]
14. Yu, H.; Wang, J.; Yu, J.X.; Wang, Y.; Chi, R.A. Adsorption performance and stability of the modified straws and their extracts of cellulose, lignin, and hemicellulose for Pb<sup>2+</sup>: pH effect. *Arab. J. Chem.* **2020**, *13*, 9019–9033. [[CrossRef](#)]
15. Al-Mahbashi, N.M.; Kutty, S.R.; Bilad, M.R.; Huda, N.; Kobun, R.; Noor, A.; Jagaba, A.H.; Al-Nini, A.; Ghaleb, A.A.; Al-dhawi, B.N. Bench-scale fixed-bed column study for the removal of dye-contaminated effluent using sewage-sludge-based biochar. *Sustainability* **2022**, *14*, 6484. [[CrossRef](#)]
16. Yadav, K.; Jagadevan, S. Influence of process parameters on synthesis of biochar by pyrolysis of biomass: An alternative source of energy. In *Recent Advances in Pyrolysis*; IntechOpen: London, UK, 2019.
17. Song, J.; He, Q.; Hu, X.; Zhang, W.; Wang, C.; Chen, R.; Wang, H.; Mosa, A. Highly efficient removal of Cr (VI) and Cu (II) by biochar derived from *Artemisia argyi* stem. *Environ. Sci. Pollut. Res.* **2019**, *26*, 13221–13234. [[CrossRef](#)]
18. Al-Rumaihi, A.; Shahbaz, M.; Mckay, G.; Mackey, H.; Al-Ansari, T. A review of pyrolysis technologies and feedstock: A blending approach for plastic and biomass towards optimum biochar yield. *Renew. Sustain. Energy Rev.* **2022**, *167*, 112715. [[CrossRef](#)]
19. Kulal, P.; Badalamoole, V. Efficient removal of dyes and heavy metal ions from waste water using Gum ghatti-graft-poly (4-acryloylmorpholine) hydrogel incorporated with magnetite nanoparticles. *J. Environ. Chem. Eng.* **2020**, *8*, 104207. [[CrossRef](#)]
20. Ahmaruzzaman, M. Nano-materials: Novel and promising adsorbents for water treatment. *Asian J. Water Environ. Pollut.* **2019**, *16*, 43–53. [[CrossRef](#)]
21. Jadhav, S.A.; Garud, H.B.; Patil, A.H.; Patil, G.D.; Patil, C.R.; Dongale, T.D.; Patil, P.S. Recent advancements in silica nanoparticles based technologies for removal of dyes from water. *Colloid Interface Sci. Commun.* **2019**, *30*, 100181. [[CrossRef](#)]
22. Liu, X.; Tian, J.; Li, Y.; Sun, N.; Mi, S.; Xie, Y.; Chen, Z. Enhanced dyes adsorption from wastewater via Fe<sub>3</sub>O<sub>4</sub> nanoparticles functionalized activated carbon. *J. Hazard. Mater.* **2019**, *373*, 397–407. [[CrossRef](#)]
23. Ourique, M.F.; Sousa, P.V.; Oliveira, A.F.; Lopes, R.P. Comparative study of the direct black removal by Fe, Cu, and Fe/Cu nanoparticles. *Environ. Sci. Pollut. Res.* **2018**, *25*, 28928–28941. [[CrossRef](#)]
24. Darwish, A.A.; Rashad, M.; AL-Aoh, H.A. Methyl orange adsorption comparison on nanoparticles: Isotherm, kinetics, and thermodynamic studies. *Dye. Pigment.* **2019**, *160*, 563–571. [[CrossRef](#)]
25. Lu, H.; Zhang, X.; Khan, S.A.; Li, W.; Wan, L. Biogenic synthesis of MnO<sub>2</sub> Nanoparticles with leaf extract of *Viola betonicifolia* for enhanced antioxidant, antimicrobial, cytotoxic, and biocompatible applications. *Front. Microbiol.* **2021**, *12*, 761084. [[CrossRef](#)]
26. Bansal, V.K.; Goel, R.K. Gastroprotective effect of *Acacia nilotica* young seedless pod extract: Role of polyphenolic constituents. *Asian Pac. J. Trop. Med.* **2012**, *5*, 523–528. [[CrossRef](#)] [[PubMed](#)]
27. Chaudhary, P.; Sharma, R.; Rawat, S.; Janmeda, P. Antipyretic medicinal plants, phytocompounds, and green nanoparticles: An updated review. *Curr. Pharm. Biotechnol.* **2023**, *24*, 23–49. [[PubMed](#)]
28. Alduraim, N.S.; Bhat, R.S.; Al-Zahrani, S.A.; Elnagar, D.M.; Alobaid, H.M.; Daghestani, M.H. Anticancer and Antimicrobial Activity of Silver Nanoparticles Synthesized from Pods of *Acacia nilotica*. *Processes* **2023**, *11*, 301. [[CrossRef](#)]
29. Ju, X.; Bowden, M.; Brown, E.E.; Zhang, X. An improved X-ray diffraction method for cellulose crystallinity measurement. *Carbohydr. Polym.* **2015**, *123*, 476–481. [[CrossRef](#)]

30. Ahmad, M.; Ahmad, M.; Usman, A.R.; Al-Faraj, A.S.; Abduljabbar, A.; Ok, Y.S.; Al-Wabel, M.I. Date palm waste-derived biochar composites with silica and zeolite: Synthesis, characterization and implication for carbon stability and recalcitrant potential. *Environ. Geochem. Health* **2019**, *41*, 1687–1704. [[CrossRef](#)]
31. Fetjah, D.; Ainhout, L.F.; Idardare, Z.; Ihssane, B.; Bouqbis, L. Effect of Banana-Waste Biochar and Compost Mixtures on Growth Responses and Physiological Traits of Seashore Paspalum Subjected to Six Different Water Conditions. *Sustainability* **2022**, *14*, 1541. [[CrossRef](#)]
32. Zubair, M.; Mu'azu, N.D.; Jarrah, N.; Blaisi, N.I.; Aziz, H.A.; AAl-Harhi, M. Adsorption behavior and mechanism of methylene blue, crystal violet, eriochrome black T, and methyl orange dyes onto biochar-derived date palm fronds waste produced at different pyrolysis conditions. *Water Air Soil Pollut.* **2020**, *231*, 240. [[CrossRef](#)]
33. Yun, Q.; Lu, Q.; Zhang, X.; Tan, C.; Zhang, H. Three-dimensional architectures constructed from transition-metal dichalcogenide nanomaterials for electrochemical energy storage and conversion. *Angew. Chem. Int. Ed.* **2018**, *57*, 626–646. [[CrossRef](#)]
34. Mei, J.; Liao, T.; Kou, L.; Sun, Z. Two-dimensional metal oxide nanomaterials for next-generation rechargeable batteries. *Adv. Mater.* **2017**, *29*, 1700176. [[CrossRef](#)]
35. Sannasi, V.; Subbian, K. Influence of Moringa oleifera gum on two polymorphs synthesis of MnO<sub>2</sub> and evaluation of the pseudo-capacitance activity. *J. Mater. Sci. Mater. Electron.* **2020**, *31*, 17120–17132. [[CrossRef](#)]
36. Pattnaik, D.; Kumar, S.; Bhuyan, S.K.; Mishra, S.C. Effect of carbonization temperatures on biochar formation of bamboo leaves. In *IOP Conference Series: Materials Science and Engineering*; IOP Publishing: Bristol, UK, 2018; Volume 338, p. 012054.
37. Aup-Ngoen, K.; Noipitak, M. Effect of carbon-rich biochar on mechanical properties of PLA-biochar composites. *Sustain. Chem. Pharm.* **2020**, *15*, 100204. [[CrossRef](#)]
38. Selvarajoo, A.; Oochit, D. Effect of pyrolysis temperature on product yields of palm fibre and its biochar characteristics. *Mater. Sci. Energy Technol.* **2020**, *3*, 575–583. [[CrossRef](#)]
39. Ciorîță, A.; Suci, M.; Macavei, S.; Kacso, I.; Lung, I.; Soran, M.L.; Pârnu, M. Green synthesis of Ag-MnO<sub>2</sub> nanoparticles using Chelidonium majus and Vinca minor extracts and their in vitro cytotoxicity. *Molecules* **2020**, *25*, 819. [[CrossRef](#)]
40. Diallo, A.; Tandjigora, N.; Ndiaye, S.; Jan, T.; Ahmad, I.; Maaza, M. Green synthesis of single phase hausmannite Mn<sub>3</sub>O<sub>4</sub> nanoparticles via Aspalathus linearis natural extract. *SN Appl. Sci.* **2021**, *3*, 562. [[CrossRef](#)]
41. Kubendiran, H.; Hui, D.; Pulimi, M.; Chandrasekaran, N.; Murthy, P.S.; Mukherjee, A. Removal of methyl orange from aqueous solution using SRB supported Bio-Pd/Fe NPs. *Environ. Nanotechnol. Monit. Manag.* **2021**, *16*, 100561. [[CrossRef](#)]
42. Han, L.; Xue, S.; Zhao, S.; Yan, J.; Qian, L.; Chen, M. Biochar supported nanoscale iron particles for the efficient removal of methyl orange dye in aqueous solutions. *PLoS ONE* **2015**, *10*, e0132067. [[CrossRef](#)]
43. Diao, Y.; Shan, R.; Li, M.; Gu, J.; Yuan, H.; Chen, Y. Efficient Adsorption of a Sulfonamide Antibiotic in Aqueous Solutions with N-doped Magnetic Biochar: Performance, Mechanism, and Reusability. *ACS Omega* **2022**, *8*, 879–892. [[CrossRef](#)]
44. Varma, A.K.; Thakur, L.S.; Shankar, R.; Mondal, P. Pyrolysis of wood sawdust: Effects of process parameters on products yield and characterization of products. *Waste Manag.* **2019**, *89*, 224–235. [[CrossRef](#)]
45. Van, H.T.; Nguyen, T.M.; Thao, V.T.; Vu, X.H.; Nguyen, T.V.; Nguyen, L.H. Applying activated carbon derived from coconut shell loaded by silver nanoparticles to remove methylene blue in aqueous solution. *Water Air Soil Pollut.* **2018**, *229*, 393. [[CrossRef](#)]
46. Da'na, E.; Taha, A.; Afkar, E. Green synthesis of iron nanoparticles by Acacia nilotica pods extract and its catalytic, adsorption, and antibacterial activities. *Appl. Sci.* **2018**, *8*, 1922. [[CrossRef](#)]
47. Shi, Y.; Song, G.; Li, A.; Wang, J.; Wang, H.; Sun, Y.; Ding, G. Graphene oxide-chitosan composite aerogel for adsorption of methyl orange and methylene blue: Effect of pH in single and binary systems. *Colloids Surf. A Physicochem. Eng. Asp.* **2022**, *641*, 128595. [[CrossRef](#)]
48. Zafar, M.N.; Dar, Q.; Nawaz, F.; Zafar, M.N.; Iqbal, M.; Nazar, M.F. Effective adsorptive removal of azo dyes over spherical ZnO nanoparticles. *J. Mater. Res. Technol.* **2019**, *8*, 713–725. [[CrossRef](#)]
49. Janani, B.; Al-Mohaimeed, A.M.; Raju, L.L.; Al Farraj, D.A.; Thomas, A.M.; Khan, S.S. Synthesis and characterizations of hybrid PEG-Fe<sub>3</sub>O<sub>4</sub> nanoparticles for the efficient adsorptive removal of dye and antibacterial, and antibiofilm applications. *J. Environ. Health Sci. Eng.* **2021**, *19*, 389–400. [[CrossRef](#)] [[PubMed](#)]
50. Zhang, B.; Wang, D. Preparation of biomass activated carbon supported nanoscale zero-valent iron (nZVI) and its application in decolorization of methyl orange from aqueous solution. *Water* **2019**, *11*, 1671. [[CrossRef](#)]
51. Arshadi, M.; SalimiVahid, F.; Salvacion, J.W.; Soleymanzadeh, M. Adsorption studies of methyl orange on an immobilized Mn-nanoparticle: Kinetic and thermodynamic. *RSC Adv.* **2014**, *4*, 16005–16017. [[CrossRef](#)]
52. Yao, Y.; Bing, H.; Feifei, X.; Xiaofeng, C. Equilibrium and kinetic studies of methyl orange adsorption on multiwalled carbon nanotubes. *Chem. Eng. J.* **2011**, *170*, 82–89. [[CrossRef](#)]
53. Chen, S.; Zhang, J.; Zhang, C.; Yue, Q.; Li, Y.; Li, C. Equilibrium and kinetic studies of methyl orange and methyl violet adsorption on activated carbon derived from Phragmites australis. *Desalination* **2010**, *252*, 149–156. [[CrossRef](#)]
54. Zhang, B.; Wu, Y.; Cha, L. Removal of methyl orange dye using activated biochar derived from pomelo peel wastes: Performance, isotherm, and kinetic studies. *J. Dispers. Sci. Technol.* **2019**, *41*, 125–136. [[CrossRef](#)]
55. Zhu, H.Y.; Jiang, R.; Xiao, L.; Zeng, G.M. Preparation, characterization, adsorption kinetics and thermodynamics of novel magnetic chitosan enwrapping nanosized  $\gamma$ -Fe<sub>2</sub>O<sub>3</sub> and multi-walled carbon nanotubes with enhanced adsorption properties for methyl orange. *Bioresour. Technol.* **2010**, *101*, 5063–5069. [[CrossRef](#)]

56. Gapusan, R.B.; Balela, M.D. Adsorption of anionic methyl orange dye and lead (II) heavy metal ion by polyaniline-kapok fiber nanocomposite. *Mater. Chem. Phys.* **2020**, *243*, 122682. [[CrossRef](#)]
57. Tripathi, M.; Sahu, J.N.; Ganesan, P. Effect of process parameters on production of biochar from biomass waste through pyrolysis: A review. *Renew. Sustain. Energy Rev.* **2016**, *55*, 467–481. [[CrossRef](#)]

**Disclaimer/Publisher's Note:** The statements, opinions and data contained in all publications are solely those of the individual author(s) and contributor(s) and not of MDPI and/or the editor(s). MDPI and/or the editor(s) disclaim responsibility for any injury to people or property resulting from any ideas, methods, instructions or products referred to in the content.